

# Characterization of Calcium Titanate–Magnesium Titanate Eutectic by Scanning Microwave Microscopy

Qinxin Zhang<sup>\*,†</sup> and Paul J. McGinn<sup>\*</sup>

Department of Chemical and Biomolecular Engineering, Center for Molecularly Engineered Materials, University of Notre Dame, Notre Dame, Indiana 46556

**Microstructure and dielectric properties in a CaTiO<sub>3</sub> (CT)–MgTiO<sub>3</sub> (MT) diffusion couple were studied by scanning electron microscopy (SEM) and near-field scanning microwave microscopy (SMM). Complex microstructures containing Mg<sub>2</sub>TiO<sub>4</sub> (M2T) and MgTi<sub>2</sub>O<sub>5</sub> (MT2) phases as well as eutectic structures of CT–MT and MT<sub>2</sub>–CT developed during cooling from the melt. Variations in the local dielectric properties observed in SMM images are correlated with the microstructures characterized by SEM/EDS. The SMM characterization clearly distinguished low-dielectric-constant MT and high-dielectric-constant CT phases. The M2T, MT, and MT<sub>2</sub> phases have similar dielectric properties, and were more difficult to distinguish in the SMM. The phase development during melting and solidification, and SMM imaging limitations are discussed.**

## I. Introduction

MICROWAVE materials with reasonably high permittivity ( $\epsilon_r > 20$ ), high-quality factor ( $Q$ ), and good temperature stability ( $\tau_r \approx 0$ ) are of commercial interest as dielectric resonators, oscillators, capacitors, filters, and patch antennae for microwave communication applications. A well-known material for temperature-compensating-type capacitors is made of a mixture of MgTiO<sub>3</sub> (MT) and CaTiO<sub>3</sub> (CT) ceramics (CaTiO<sub>3</sub>–MgTiO<sub>3</sub>, hereafter referred to as CMT). By varying the relative concentration of MT and CT, one can tailor the dielectric behavior.

In the microwave frequency range, magnesium titanate (gierite, MgTiO<sub>3</sub>) has a low  $\epsilon_r$  ( $\sim 17$ ), high  $Q \times f$  ( $\sim 7000$ – $20\,800$  at 7 GHz), and a negative  $\tau_r$  ( $-45$  ppm/°C).<sup>1</sup> Calcium titanate (perovskite, CaTiO<sub>3</sub>) has a high  $\epsilon_r$  ( $\sim 170$ ), moderate  $Q \times f$  ( $\sim 1800$ – $3000$  at 7 GHz), and a large positive  $\tau_r$  ( $+800$  ppm/°C).<sup>1</sup> Addition of 5 mol% CaTiO<sub>3</sub> to MgTiO<sub>3</sub> yields a (Mg<sub>0.95</sub>Ca<sub>0.05</sub>)TiO<sub>3</sub> ceramic that exhibits  $\epsilon_r \sim 21$ ,  $Q \times f$  values  $\sim 56\,000$  at 7 GHz, and a  $\tau_r$  value of  $\sim 0$  ppm/°C.<sup>1</sup>

The sintering temperature to densify mixed CT–MT ceramics is as high as 1400°C. Compared with solid-state sintering, the presence of a liquid phase leads to improved densification through enhanced particle rearrangement and transport through the liquid.<sup>2</sup> A CT–MT mixture melts and forms a eutectic liquid at 1462.5°C, which, under proper solidification conditions, can be used to achieve a highly dense product. For example, (Mg<sub>0.95</sub>Ca<sub>0.05</sub>)TiO<sub>3</sub> single-crystal fibers with anisotropic dielectric properties have been grown from a CMT eutectic melt by laser-heated pedestal growth processing at 1650°–1720°C.<sup>3</sup> During fiber growth, the presence of intermediate phases of MgTi<sub>2</sub>O<sub>5</sub> (karrooite, MT2) and Mg<sub>2</sub>TiO<sub>4</sub> (qandilite, M2T) was noted, and they were difficult to eliminate completely from the

reaction products.<sup>4</sup> But the amount of the intermediate MT<sub>2</sub> phase could be decreased at higher growth temperatures.

Rather than melting at high temperature, small additions are often used to promote liquid-phase sintering and thereby enhance densification. The additions melt or react with a small part of the major component to form a eutectic liquid on heating. In the (Mg<sub>0.95</sub>Ca<sub>0.05</sub>)TiO<sub>3</sub> system, many researchers have promoted densification by using a range of additives, including La<sub>2</sub>O<sub>3</sub>, Cr<sub>2</sub>O<sub>3</sub>,<sup>5</sup> CuO,<sup>6</sup> B<sub>2</sub>O<sub>3</sub>,<sup>7,8</sup> V<sub>2</sub>O<sub>5</sub>,<sup>8</sup> or Bi<sub>2</sub>O<sub>3</sub>,<sup>9</sup> to lower the sintering temperature. Additions of La<sub>2</sub>O<sub>3</sub> or V<sub>2</sub>O<sub>5</sub> resulted in the formation of MgTi<sub>2</sub>O<sub>5</sub> and La<sub>2</sub>Ti<sub>2</sub>O<sub>7</sub> or Ca<sub>5</sub>Mg<sub>4</sub>V<sub>6</sub>O<sub>24</sub> phases during the sintering process, which decreased the dielectric properties significantly. Because of the common use of liquid-phase processing in this system, study of phase formation as a result of melting and solidification is relevant to understanding the permittivity variation and the microstructures of the CT–MT system.

In the present work, this is accomplished through the use of an MgTiO<sub>3</sub>–CaTiO<sub>3</sub> diffusion couple to simulate what occurs at the interface between CT and MT grains during processing in the presence of a liquid, permitting the phase evolution to be followed. The nondestructive mapping technique of near-field scanning microwave microscopy (SMM) permits the characterization of the local effects of inhomogeneities and defects in crystals. This has been shown to be effective for the characterization of local dielectric variations in bulk ceramics.<sup>10–12</sup> Here, we examine a much more complex microstructure by combining characterization by backscattered electron SEM/EDS with SMM to correlate the microstructure with the local dielectric properties.

## II. Experimental Procedure

The precursor powders used in this work were CaCO<sub>3</sub> (99.95%, metal basis, Alfa Aesar, Ward Hill, MA), TiO<sub>2</sub> (99.9%, Aldrich, Milwaukee, WI), and MgTiO<sub>3</sub> (99%, metal basis, Alfa Aesar). CaTiO<sub>3</sub> powder was prepared by a standard solid-state reaction method. CaCO<sub>3</sub> and TiO<sub>2</sub> were mixed in a 1:1 molar ratio and milled with ZrO<sub>2</sub> balls in ethanol for 12 h, dried, pressed into pellets, calcined at 1300°C for 10 h in air, ground, and reacted. Routine powder XRD results showed that the reaction was completed. The CT pellets were in turn ground and ball milled for 30 min. The CT powder was packed into a latex tube and hydrostatically pressed into a rod of about  $\phi = 0.6 \times 25$  cm under 70 MPa hydraulic pressure (CD-10, Riken Kiki Co. Ltd., Tokyo, Japan). The resulting rod was sintered at 1300°C in a vertical SiC furnace (Crystal Systems Inc., Yamanashi, Japan) for 10 h. The MT powder was similarly hydrostatically pressed into a rod and sintered in the vertical SiC furnace at 1300°C in air for 10 h. One end of the sintered CT rod was cut off and the surface of the remaining rod was polished. The CT rod was mounted vertically in an optical floating zone furnace (FZ-T-10000-H-VI-VP, Crystal Systems Inc.) as the supporting rod. A 5 mm tall pellet was sliced from sintered MT rod and the cut surface was polished. This polished MT pellet was set on top of the CT rod with the polished surfaces facing each other. The interface of the diffusion couple was placed at the focal point of four 300 W tungsten halide lamps by adjusting the position of

D. Johnson—contributing editor

Manuscript No. 21723. Received April 19, 2006; approved July 9, 2006.

Supported by Indiana 21st Century Research and Technology Fund.

<sup>\*</sup>Member, American Ceramic Society.

<sup>†</sup>Author to whom correspondence should be addressed. e-mail: qzhang@nd.edu

the supporting rod. The rod was rotated at 20 rpm to heat the interface as uniformly as possible. While observing the interface with a video camera system, the temperature was slowly ramped up in a flowing air ambient ( $\sim 5^\circ\text{C}/\text{min}$ ) until liquid appeared at the joint, which was discernable by a sample color change. The estimated temperature was about  $1460^\circ$  to  $1500^\circ\text{C}$ . The diffusion couple was maintained at this temperature for about 10 min to promote liquid diffusion. The temperature was then quickly ramped down below the freezing temperature to quench the interfacial reaction. The diffusion couple was later sliced from the CT rod and mounted into epoxy resin. The cross section of the interdiffusion region was carefully polished for further characterization by polarized optical microscopy (Olympus BX61, Nashua, NH), X-ray powder diffraction (Scintag X1, Scintag Inc., Cupertino, CA), near-field scanning microwave microscopy (EMP2001, Ariel Technologies Inc., Moraga, CA), and scanning electron microscopy (SEM; Model Evo 50, Carl Zeiss SMT Inc., Thornwood, NY) in a system equipped with an energy-dispersive spectrometer (EDS; INCA Microanalysis system, Oxford Instruments, High Wycombe, U.K.). For SEM and EDS analysis, the polished surface was coated with carbon to reduce sample charging.

A schematic diagram of the SMM used in this work is described elsewhere.<sup>10</sup> The SMM is designed to shield off the far-field propagating electromagnetic waves and utilize the evanescent microwaves generated at the end of a tungsten fine tip. By moving the tip/resonator assembly close to an object, the interaction between the evanescent microwaves and the object can be recorded to map the changes in the cavity resonant frequency  $f_r$  and quality factor  $Q$  as a function of position, and thereby construct surface SMM images. When the tip contacts a sample, the sample dielectric properties on the cavity resonant frequency can be described in terms of the cavity resonant frequency. Namely, a lower cavity resonant frequency means a higher sample dielectric constant. The method to relate quantitatively the resonant frequency to dielectric constant is described elsewhere.<sup>10</sup> The  $f_r$  and  $Q$  are sensitive to the gap between the tip and the ceramic sample surface.<sup>10–12</sup> In this investigation, the sample was polished down to a  $0.5\ \mu\text{m}$  surface finish to minimize surface roughness effects. All scans were performed with the SMM probe tip in contact with the sample surface during scanning (soft-contact mode) to boost the signal intensity and sensitivity.

### III. Results and Discussion

The microstructures of the polished cross section of the CT–MT diffusion couple were characterized by optical microscopy and backscattered electron SEM, while the local surface dielectric properties were mapped with SMM. The phases were identified by EDS analysis and XRD. The possible phase evolution during the melting and solidification is discussed below.

#### (1) Optical Observation and X-Ray Powder Diffraction

An overall optical image of the polished cross section of the CT–MT diffusion couple, as can be seen in Fig. 1, revealed that there are several cracks in the CT region close to the interface area, but no cracks in the MT region. Thermal stresses originating from the different thermal expansion coefficients of  $\text{MgTiO}_3$  ( $10\ \text{ppm}/^\circ\text{C}$ ) and  $\text{CaTiO}_3$  ( $14\ \text{ppm}/^\circ\text{C}$ ),<sup>13</sup> thermal stresses resulting from the temperature gradient between the hot zone and the supporting rod, and the rapid cooling rate used in the experiment could all contribute to the formation of cracks. Previous experiments involving two stacked layers of 1" MT and CT pellets sintered at  $1400^\circ\text{C}$  for 10 h in a conventional furnace and cooled down at a rate of  $1^\circ\text{C}/\text{min}$  produced cracks along the MT layer instead of the CT layer. A study of complex layered structures with different configurations of MT/CT ratios and layers also indicated that cracks were observed only in MT layers.<sup>13</sup> In the present study, formation of cracks by differing thermal expansion coefficients was minimized as the MT pellet was relatively small and thin. Hence, the crack formation was probably

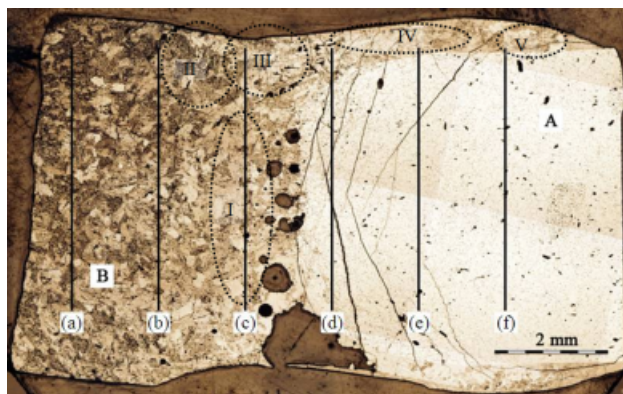


**Fig. 1.** An overall optical image of a CT–MT diffusion couple cross section, which shows the  $\text{CaTiO}_3$  precursor region (A), the  $\text{MgTiO}_3$  precursor region (B), the porous interdiffusion layer, and the frozen melt covering the CT rod. The overlaid lines indicate the relative locations for sequential X-ray diffraction characterizations. The labeled regions I–V indicate the different locations for microstructure characterization.

because of the sharp temperature gradient between the hot zone and the supporting rod outside the heating zone, and the rapid cooling rate after the heat treatment.

The crystallographic phases along the diffusion couple were characterized by X-ray powder diffraction scans along the diffusion couple. The XRD characterization was performed at the six locations denoted in Fig. 1 (labeled (a)–(f)), with an interval distance of  $0.06''$ . The sample was moved by a motor translation stage and the XRD patterns were recorded sequentially after each movement to compare the phase changes across the couple. After quick solidification, the composition gradients of MT and CT are observed in the XRD patterns in Fig. 2. The MT dominated at (a), while CT was the dominant phase at (f). The approximated volume ratio of MT to CT, which was calculated using Jade 7 X-ray analysis, gradually decreased from 5.84 at (b), through 2.31 at (c), 0.37 at (d), to 0.29 at (e), indicating the interdiffusion of the MT and CT. The characteristic XRD lines of the precursor MT and CT materials can be observed clearly in Fig. 2. The MT2 phase is observed in each location, while the M2T phase is only observed in locations (c) and (d), which are in the interdiffusion region. The XRD patterns of the MT powder used and the as-sintered MT rod confirmed that there was trace MT2 in the precursor MT phase, which also could be observed in Fig. 2(a). The presence of trace MT2 in the precursor MT rod may not affect the melting temperature

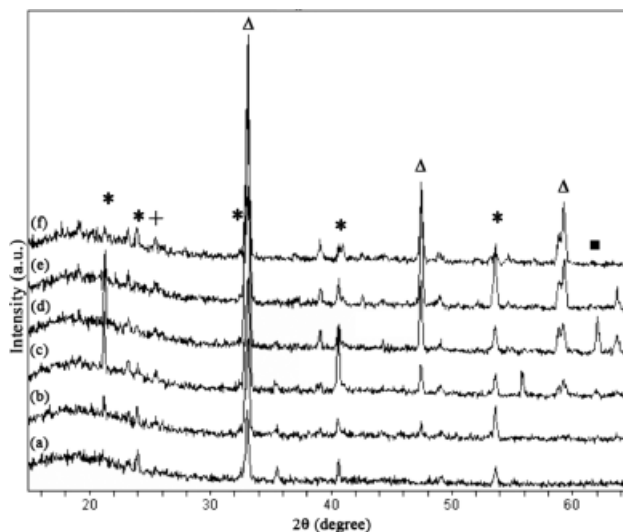


**Fig. 2.** X-ray powder diffraction patterns at the six locations, (a)–(f), illustrated in Fig. 1 (\*, MT;  $\Delta$ , CT; +, MT2;  $\blacksquare$ , M2T).

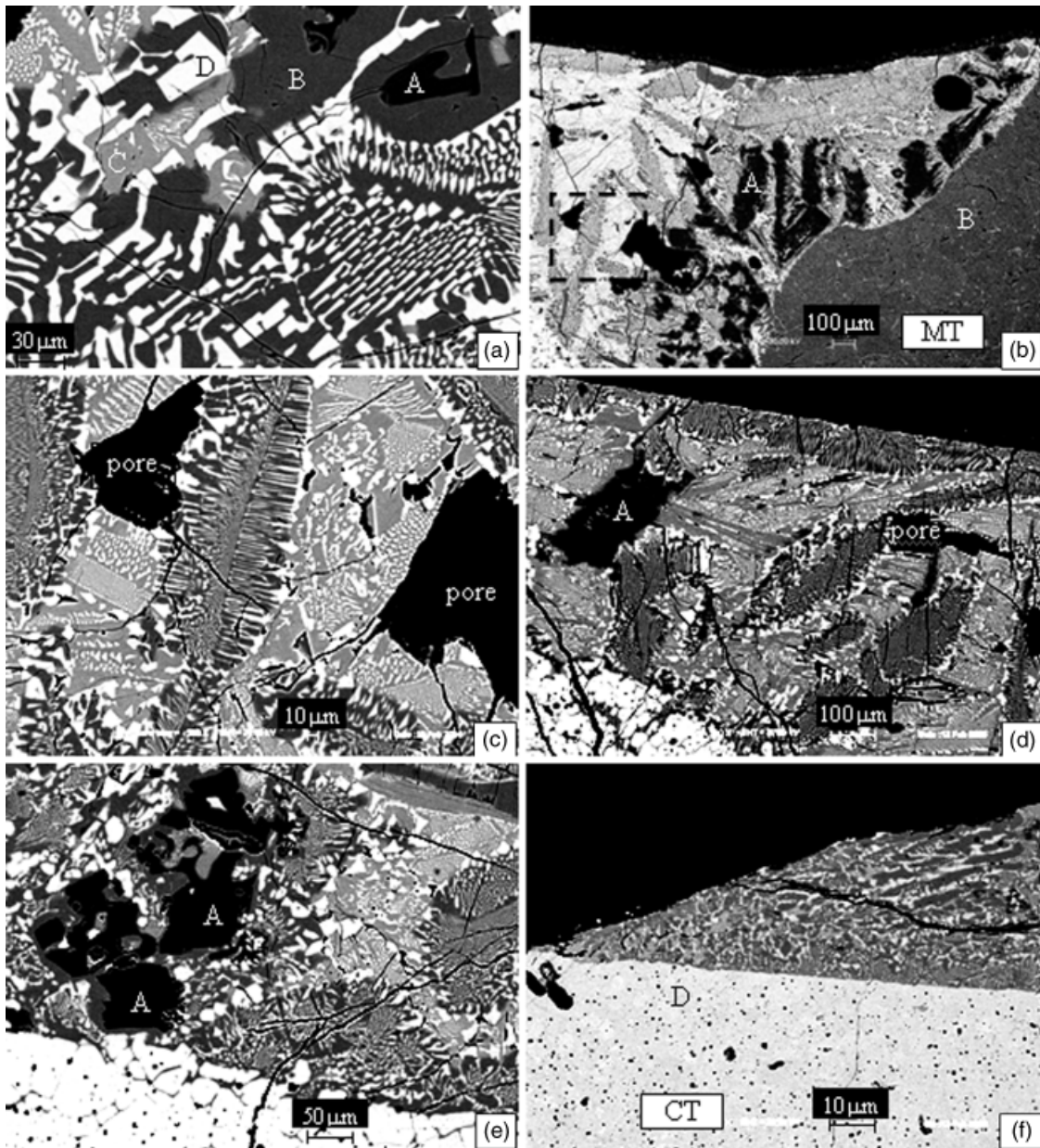


**Fig. 3.** Backscattered scanning electron microscopy images that show the microstructure of the CMT diffusion couple in different regions (identified in Fig. 1): (a) region I; (b) large M2T clusters in region II; (c) the area of (b) bounded by the box; (d) eutectic microstructures in region III; (e) region IV; (f) region V. The phases including M2T (dark, A), MT (gray, B), MT2 (light gray, C), and CT (white, D), the eutectic phases of MT–CT, MT2–CT, as well as the pores and cracks (black lines) are observed.

of the diffusion couple as the MT2 will not necessarily contact CT particles at the initial state.

## (2) Backscattered Electron SEM/EDS

In order to reveal the microstructures across the diffusion couple, the cross section of the diffusion couple was characterized by backscattered electron SEM (BSE–SEM), and the phases were analyzed by EDS. The five regions that were analyzed are labeled in Fig. 1 as regions I–V. Region I is close to the contact interface of the two rods. The interface between the frozen melt and the MT region is in region II. Regions III to V, respectively, are the precipitate at the outer edge of the CT–MT joint, the coating that developed on the CT rod, and the furthest region wetted by the liquid on the CT rod. Backscattered electron SEM images of these five regions are shown in Fig. 3. The results of EDS analysis indicate that the dark phase (A), gray phase (B), light gray phase (C), and white phase (D) are M2T, MT, MT2, and CT, respectively. The backscattered SEM

images show that the impurity MT2 and M2T phases coexist with the precursor CT and MT phases in the frozen melt. The M2T phase is inhomogeneously distributed in the precipitate. The M2T particles aggregated as large clusters near the precursor MT region and in the diffusion interface region [Fig. 3(a) and (b)]. Occasionally, M2T clusters were also found inside the frozen melt in region IV [Fig. 3(e)]. This observation is consistent with the XRD results in Fig. 2, which show that the M2T phase is found in the interdiffusion region. The SEM images at a higher magnification revealed that the M2T was embedded in the MT continuous matrix phase. Figures 3(b) and (c) show that both CT–MT and CT–MT2 eutectic structures developed in the frozen melt. A surface layer of an MT–CT eutectic phase could also be observed in regions III and V, as shown in Figs. 3(d) and (f). The CT particles within the eutectic phases appeared as needles, triangular spikes, short rods, or other geometries, while the MT and MT2 phases were continuous matrix phases.

The liquid phase from the interface wetted the MT grain boundaries. MT subsequently precipitates from the liquid onto

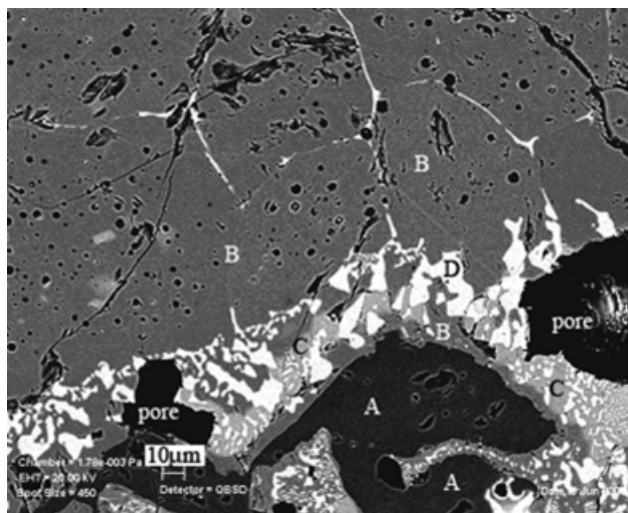


**Fig. 4.** Backscattered electron scanning electron microscopy image in region I, showing the CT-rich grain boundaries on the MT side of the joint. The eutectic phase of MT2–CT, large M2T clusters (A), and the individual phases of MT (B), M2T (light gray, C) and CT (white, D), as well as the pores and cracks (black) can be observed.

the MT grains, leaving the CT phase (white) along the MT grain boundaries as can be seen in Fig. 4. Similar liquid phase penetration occurred on the CT precursor side. The MT phase occupied the grain boundaries of the CT grains of the region shown in Fig. 5. Coarsening of the microstructure because of the presence of the liquid is obvious.

### (3) Phase Evolution During Solidification

The presence of a liquid phase had a noticeable influence on both diffusion rates and the contact areas between phases. When the volume of liquid was sufficient, the liquid spread out of the molten zone and wetted the surface of the supporting rod. The microstructure inside the frozen–melt layer suggests the possible phase evolution sequence during the non-equilibrium liquid solidification. The phase diagram for the MT–CT system [Fig. 6(a)] shows that the eutectic temperature of an MT-rich CT–MT mixture is around 1462.5°C.<sup>14</sup> When the temperature was above the eutectic temperature, eutectic liquid of CT–MT formed.

As shown in the ternary TiO<sub>2</sub>–CT–MT phase diagram [Fig. 6(b)],<sup>14</sup> during freezing the liquid composition will become more Ti rich, moving down the eutectic trough toward the tern-

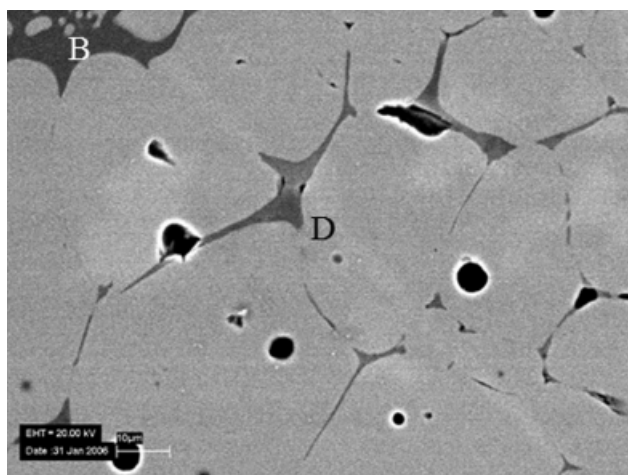


**Fig. 5.** Backscattered electron scanning electron microscopy image, which shows that the MT (B) penetrates the grain boundaries of the CT (D) inside the CT rod, which is close to region IV.

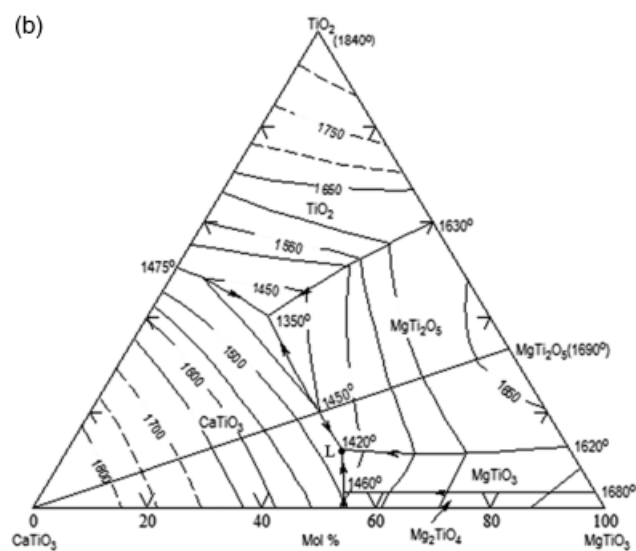
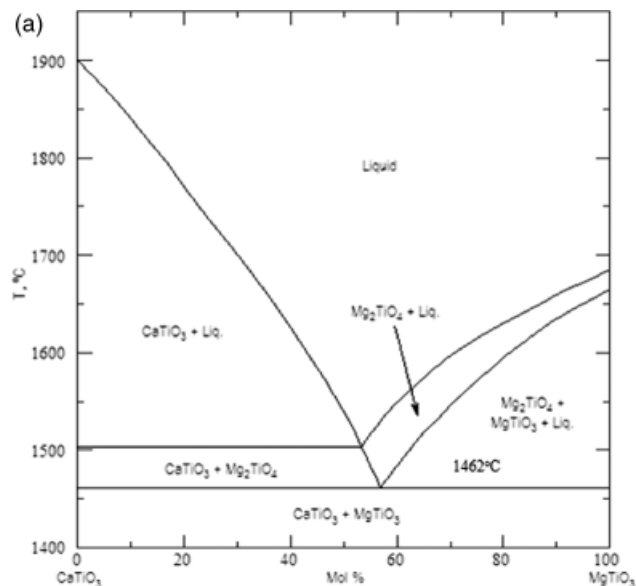


**Fig. 6.** Phase diagrams for (a) a CT–MT system, and (b) a ternary CT–MT–TiO<sub>2</sub> system.<sup>14</sup>

ary eutectic point (L) at 21.1%Ca–25.7%Mg–53.2%Ti–O<sub>x</sub> (mol). As a result, the solid phases in equilibrium will change with decreasing temperature from the initial CT+MT, to CT+MT+M2T, and finally to CT+MT+MT2 at the 1420°C freezing point.

The actual local liquid composition will be affected by the local liquid/solid ratio and the temperature. Surface tension, temperature gradients, and gravity permit the liquid to flow out from the hot zone and spread over the outside surface of the adjacent CT-supporting rod. Liquid transport away from the hot zone, the quick cooling rate, and the large temperature gradient parallel to the rod axis all result in the liquid solidifying under nonequilibrium conditions. SEM images of the interface of the frozen melt and the CT precursor region are shown in Figs. 3(e) and (f). The liquid penetrated into the CT or MT particles, and the CT or MT solid dominated the local equilibrium, and so prevented formation of the impurities M2T and MT2. The SEM images in Figs. 4 and 5 confirmed that no impurity M2T or MT2 precipitate was found in the precursor CT and MT regions.

Liquid wets the surface of the CT rod and flows along the rod (and the temperature gradient) until it reaches a sufficiently cool region where solidification will occur. SEM examination confirmed that the eutectic shell on the support rod is the CT–MT

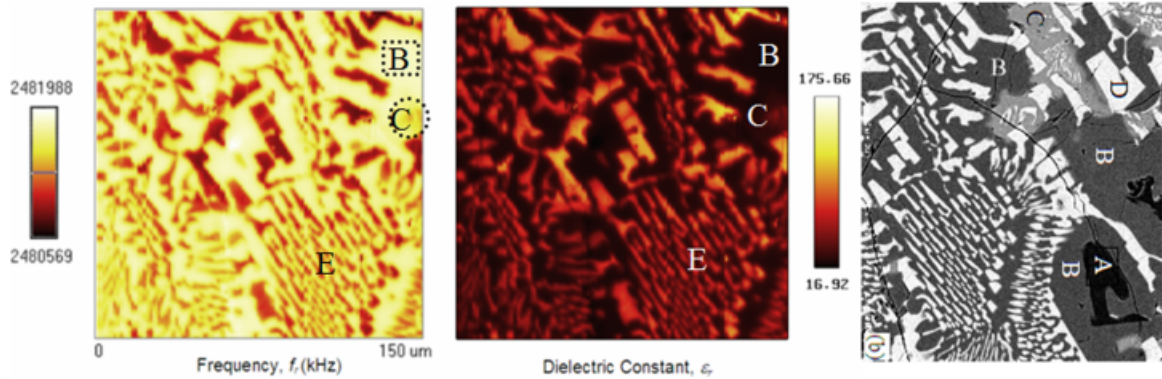


**Fig. 7.** Scanning microwave microscopy resonant frequency (left) and dielectric constant (center) images that show the dielectric properties' variation because of the range of phases present near the interface region. The corresponding scanning electron microscopy image is shown on the right. The phases including M2T (A), MT (B), MT2 (C), CT (D), and eutectic MT–CT (E) phases are observed.

eutectic, resulting in the surface eutectic layer seen in the SEM images of Fig. 3. The nonequilibrium solidification resulted in the coexistence of the MT2, M2T, MT, and CT phases along with the eutectic MT–CT and MT2–CT structures in the final frozen melt, and several different morphologies of the CT phase in the microstructure.

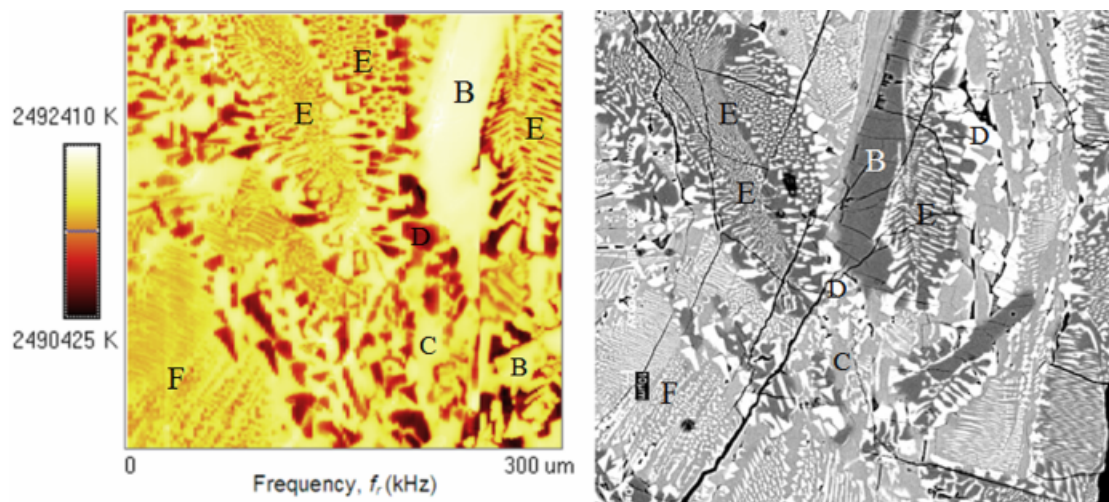
#### (4) SMM Results

The optical and SEM images show that the polished surface of the diffusion couple is porous. As all of the SMM scans in the present work were performed with the probe tip in contact with the surface during the scan period, the porous surface limited SMM scans to areas with few defects. The resonant frequency and dielectric constant SMM images at different locations of the interdiffusion area are shown in Figs. 7–10. The contrast in the dielectric constant images shows the dielectric constant variation caused by the presence of different phases. In order to correlate the dielectric properties' variation with the microstructure, the corresponding SEM images are shown along with the SMM images. Comparing the SMM and SEM images, the small long cracks that are clearly observed in the SEM image are hard to distinguish from the other features in the SMM image because of the high contrast between the CT and MT phases. In a microstructure with a more narrow range of dielectric constant phases, the cracks would be more apparent. The high dielectric constant  $\text{CaTiO}_3$  phase with  $\epsilon_r \sim 170$  is observed as red in the resonant frequency images or a bright red color in dielectric constant images. The Mg–Ti–O phases, including M2T, MT,

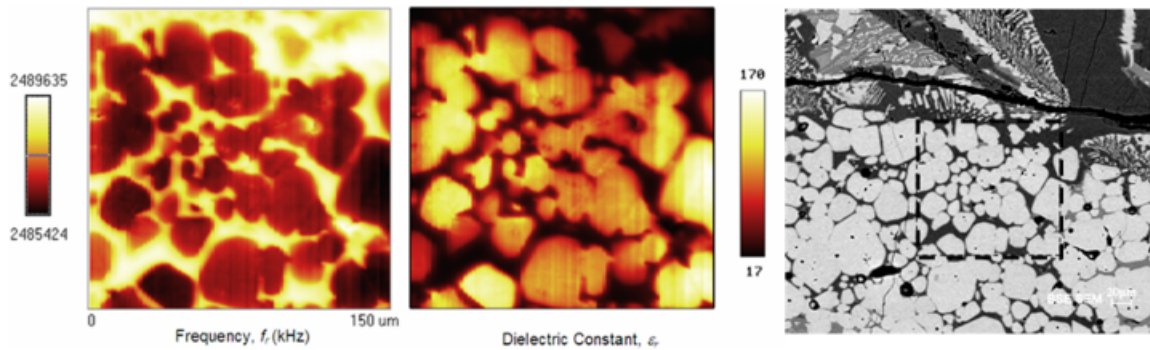
and MT2, having much lower dielectric constants than CT, appear as a light yellow color in the resonant frequency images and are dark in the dielectric constant images. Figure 7 shows SMM images inside region I and the corresponding SEM image, which is the image in Fig. 3(a) rotated  $90^\circ$  clockwise. The eutectic MT–CT phase and individual MT and CT particles could be distinguished in both the SMM and SEM images. Smearing of phase boundaries is evident when comparing SMM and SEM images. Figure 8 shows the SMM image and corresponding SEM image of region IV. Both of the eutectic MT–CT and eutectic MT2–CT phases are apparent in the SEM and SMM images. The dielectric constant of MT2 (phase C) has a slightly higher dielectric constant than MT (phase B).

Figure 7 shows SMM resonant frequency (left) and dielectric constant (center) images that show the dielectric properties variation because of the range of phases present near the interface region. The corresponding SEM image is shown on the right. The phases including M2T (A), MT (B), MT2 (C), CT (D), and eutectic MT–CT (E) phases are observed.

Figure 9 shows the SMM images scanned in the precursor CT area in region I. The high dielectric-constant grains belong to the CT phase, while the low-dielectric-constant phase along the grain boundaries is the MT phase. The CT grains have a relatively uniform color in the SMM images, indicating a uniform dielectric constant around 170. The small rod-like CT phase in Figs. 7 and 8, however, appears to be a lower dielectric constant phase than the large CT grains. For example, the CT dots or rods of the eutectic MT2–CT phase F in Fig. 8 show a lower dielectric constant than the CT rods or triangles of the eutectic



**Fig. 8.** Resonant frequency (left) and corresponding BSE scanning electron microscopy (right) images, which show both CT–MT and CT–MT2 eutectic microstructures in region IV. The phases labeled B–F are MT, MT2, CT, eutectic MT–CT, and eutectic MT2–CT phases, respectively.



**Fig. 9.** SMM resonant frequency (left) and dielectric constant (center) images of region I near the interface. The corresponding scanning electron microscopy (SEM) image is shown on the right. The scan was performed in the region indicated by the box in the scanning electron microscopy image.

MT–CT phase E and non-eutectic CT phase D. This results from having an SMM tip size (5–10  $\mu\text{m}$ ) that is much larger than some of the eutectic microstructural features. Thus, the SMM image constructed from the average signal collected by the SMM tip shows smearing of microstructural feature boundaries, and does not have as high a resolution as the SEM image. Moreover, apparent dielectric constant values are also affected by the tip size relative to microstructure feature size. For example, as the  $\text{CaTiO}_3$  particles are surrounded by lower dielectric constant  $\text{MgTiO}_3$ , the SMM probe will collect the signals from both phases at the boundaries, yielding a slightly lower dielectric constant near the boundaries of the CT grains. As shown in the SMM images of Fig. 9, each large CT particle includes a boundary region, which appears to have a lower dielectric constant than the center of CT particles. When the CT particle is smaller than some critical size, which will depend on the tip size and a feature's dielectric properties, the dielectric constant of these CT particles will be lower than those of large CT particles. The same situation arises for the CT phase surrounded by the MT2 phase.

Another SMM imaging artifact is observed for the MT2 and M2T phases, which have dielectric constants very similar to the MT phase, and are all much lower than the CT phase. As a result, it is hard to distinguish the MT2, MT, and M2T phases from each other in the SMM images, as the relative contrast between them is much smaller than the contrast between the CT and MT phases. By comparing the SMM images of Fig. 7 with the corresponding BSE–SEM image, a small amount of CT embedded in the MT2 phase can be located in the circled region of

Fig. 7, while a pure MT phase is located in the square region. The SMM images in Figs. 7 and 8 indicate that the MT2 has a slightly higher dielectric constant than the MT phase. In addition, the dashed oval regions in Fig. 10 indicate regions with coexisting M2T and MT according to the BSE–SEM image in Fig. 3(a). The SMM image in Fig. 10 indicates that the M2T phase has a dielectric constant very close to the MT phase. Our previous study on co-fired M2T–MT–CT ceramics indicates that the MT has a slightly lower dielectric constant than the M2T phase.<sup>11</sup>

#### IV. Conclusions

A CT–MT diffusion couple was melted and quickly solidified in an optical floating zone furnace to study microstructure development. SMM and SEM were used to correlate the local dielectric properties' variations with the microstructures in different regions of the diffusion couple. There are two different eutectic structures, CT–MT and CT–MT2, found after solidification. SMM images showed the range of dielectric properties of the various phases in the complex microstructures. CT with a high dielectric constant could be clearly distinguished from the low-dielectric-constant MT in the SMM images. The MT2 and M2T phases had dielectric properties very similar to the MT phase, exhibiting less contrast and making them harder to distinguish from each other in the SMM. Limitations in SMM imaging because of the 5–10  $\mu\text{m}$  tip size resulted in smearing of the phase boundaries of small microstructure features, limiting the achievable resolution.

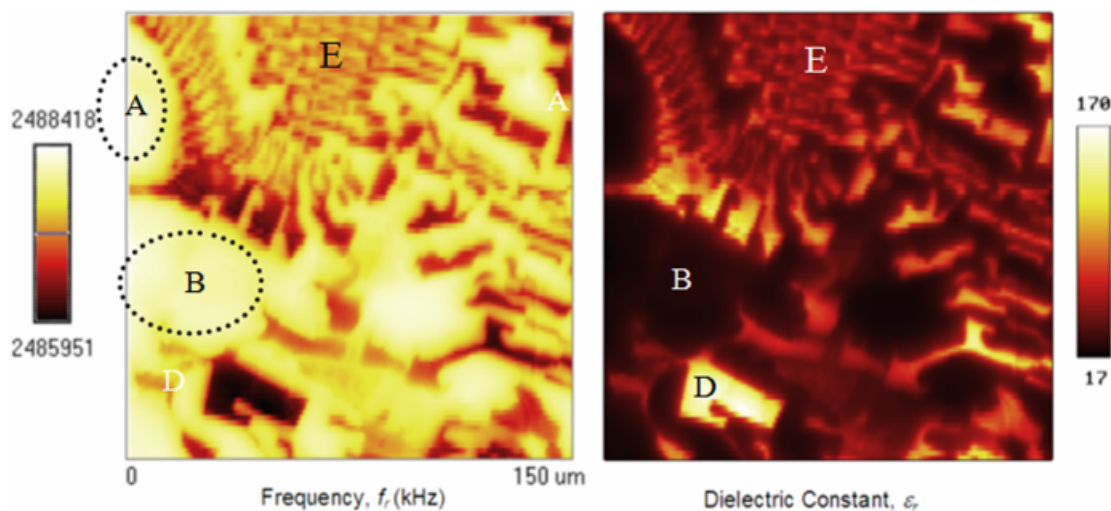


**Fig. 10.** Scanning microwave microscopy resonant frequency and dielectric constant images of the MT–CT eutectic in region I (compare with scanning electron microscopy image in Fig. 3(a)). The phases including M2T (A), MT (B), CT (D), and eutectic MT–CT (E) are denoted in the scanning microwave microscopy images.

## References

- <sup>1</sup>K. Wakino, "Recent Development of Dielectric Resonator Materials and Filters in Japan," *Ferroelectrics*, **91**, 69–86 (1989).
- <sup>2</sup>M. N. Rahaman, *Ceramic Processing and Sintering*, 2nd Edition, p. 875. Marcel Dekker Inc., New York, 2003.
- <sup>3</sup>Y. J. Jiang, R. Y. Guo, and A. S. Bhalla, "LHPG Grown Crystal Fibers of MgTiO<sub>3</sub>–CaTiO<sub>3</sub> Eutectic System," *J. Phys. Chem. Solids*, **59** [5] 611–5 (1998).
- <sup>4</sup>I. Shindo, "Determination of the Phase-Diagram by the Slow Cooling Float Zone Method—the System MgO–TiO<sub>2</sub>," *J. Cryst. Growth*, **50** [4] 839–51 (1980).
- <sup>5</sup>V. M. Ferreira, F. Azough, R. Freer, and J. L. Baptista, "The effect of Cr and La on MgTiO<sub>3</sub> and MgTiO<sub>3</sub>–CaTiO<sub>3</sub> microwave dielectric ceramics," *J. Mater. Res.*, **12** [12] 3293–9 (1997).
- <sup>6</sup>C. L. Huang, C. L. Pan, and S. J. Shium, "Liquid Phase Sintering of MgTiO<sub>3</sub>–CaTiO<sub>3</sub> Microwave Dielectric Ceramics," *Mater. Chem. Phys.*, **78** [1] 111–5 (2003).
- <sup>7</sup>C. L. Huang and M. H. Weng, "Improved High Q Value of MgTiO<sub>3</sub>–CaTiO<sub>3</sub> Microwave Dielectric Ceramics at Low Sintering Temperature," *Mater. Res. Bull.*, **36** [15] 2741–50 (2001).
- <sup>8</sup>H. Yamamoto, A. Koga, S. Shibagaki, and N. Ichinose, "Low Temperature Firing of MgTiO<sub>3</sub>–CaTiO<sub>3</sub> Microwave Dielectric Ceramics Modified with B<sub>2</sub>O<sub>3</sub> or V<sub>2</sub>O<sub>5</sub>," *J. Ceram. Soc. Jpn.*, **106** [3] 339–43 (1998).
- <sup>9</sup>C. L. Huang and C. L. Pan, "Low-Temperature Sintering and Microwave Dielectric Properties of (1–x)MgTiO<sub>3</sub>–xCaTiO<sub>3</sub> Ceramics Using Bismuth Addition," *Jpn. J. Appl. Phys.*, **41** [2A] 707–11 (2002).
- <sup>10</sup>Q. X. Zhang and P. J. McGinn, "Imaging of Oxide Dielectrics by Near-Field Microwave Microscopy," *J. Eur. Ceram. Soc.*, **25** [4] 407–16 (2005).
- <sup>11</sup>Z. N. Wang, J. W. Halloran, Q. X. Zhang, and P. J. McGinn, "Variable Dielectrics in the Calcium Magnesium Titanate System Characterized with Scanning Microwave Microscopy," *J. Am. Ceram. Soc.*, **89** [5] 1610–4 (2006).
- <sup>12</sup>Q. X. Zhang and P. J. McGinn, "Microstructure and Dielectric Properties of a LaAlO<sub>3</sub>–TiO<sub>2</sub> Diffusion Couple," *J. Am. Ceram. Soc.*, **89** [5] 1687–93 (2006).
- <sup>13</sup>X. M. Chen, L. Li, and X. Q. Liu, "Layered Complex Structures of MgTiO<sub>3</sub> and CaTiO<sub>3</sub> Dielectric Ceramics," *Mater. Sci. Eng., B*, **99** [1–3] 255–8 (2003).
- <sup>14</sup>M. A. Rouf, A. H. Cooper, and H. B. Bell, "A Study of Phase Equilibria in the System CaO–MgO–TiO<sub>2</sub>," *Trans. Br. Ceram. Soc.*, **68** [6] 263–7 (1969). *ACerS-NIST Phase Equilibria Diagrams CD-ROM Database, version 3.0* (The American Ceramic Society, Westerville, OH, 2004), Fig. 04553. □